

Article

A Free-Energy Landscape Analysis of Calmodulin Obtained from an NMR Data-Utilized Multi-Scale Divide-and-Conquer Molecular Dynamics Simulation

Hiromitsu Shimoyama *  and Yasuteru Shigeta * 

Center for Computational Sciences, University of Tsukuba, 1-1-1 Tennodai, Tsukuba 305-8577, Japan

* Correspondence: simoyama@ccs.tsukuba.ac.jp (H.S.); shigeta@ccs.tsukuba.ac.jp (Y.S.); Tel.: +81-29-853-6496 (Y.S.)

Abstract: Calmodulin (CaM) is a multifunctional calcium-binding protein, which regulates a variety of biochemical processes. CaM acts through its conformational changes and complex formation with its target enzymes. CaM consists of two globular domains (N-lobe and C-lobe) linked by an extended linker region. Upon calcium binding, the N-lobe and C-lobe undergo local conformational changes, followed by a major conformational change of the entire CaM to wrap the target enzyme. However, the regulation mechanisms, such as allosteric interactions, which regulate the large structural changes, are still unclear. In order to investigate the series of structural changes, the free-energy landscape of CaM was obtained by multi-scale divide-and-conquer molecular dynamics (MSDC-MD). The resultant free-energy landscape (FEL) shows that the Ca²⁺ bound CaM (holo-CaM) would take an experimentally famous elongated structure, which can be formed in the early stage of structural change, by breaking the inter-domain interactions. The FEL also shows that important interactions complete the structural change from the elongated structure to the ring-like structure. In addition, the FEL might give a guiding principle to predict mutational sites in CaM. In this study, it was demonstrated that the movement process of macroscopic variables on the FEL may be diffusive to some extent, and then, the MSDC-MD is suitable to the parallel computation.

Keywords: molecular dynamics simulation; calmodulin; domain motion; dynamics; conformational change; free-energy analysis



Citation: Shimoyama, H.; Shigeta, Y. A Free-Energy Landscape Analysis of Calmodulin Obtained from an NMR Data-Utilized Multi-Scale Divide-and-Conquer Molecular Dynamics Simulation. *Life* **2021**, *11*, 1241. <https://doi.org/10.3390/life11111241>

Academic Editors: Hiroshi Fujisaki and Yuichi Togashi

Received: 30 September 2021
Accepted: 10 November 2021
Published: 16 November 2021

Publisher's Note: MDPI stays neutral with regard to jurisdictional claims in published maps and institutional affiliations.



Copyright: © 2021 by the authors. Licensee MDPI, Basel, Switzerland. This article is an open access article distributed under the terms and conditions of the Creative Commons Attribution (CC BY) license (<https://creativecommons.org/licenses/by/4.0/>).

1. Introduction

Calcium ions (Ca²⁺) act as intracellular messengers that relay information within cells to regulate cellular processes [1,2]. The information of a transient Ca²⁺ signal is converted into a wide variety of biochemical changes by Ca²⁺-binding proteins (also known as Ca²⁺-sensors) through Ca²⁺-induced conformational changes [3,4]. Calmodulin (CaM) is a ubiquitous Ca²⁺-sensor found in eukaryotic cells, which activates enzymes, such as kinases and phosphatases, in a Ca²⁺-dependent manner so that it regulates various biochemical processes. In the early 1970s, the activation activity by CaM was discovered in a study of phosphodiesterase (PDE), and then its activating factor was identified as a Ca²⁺-binding protein [5–9]. Nowadays, CaM is known to be involved in various cellular processes, such as cell proliferation, apoptosis, muscle contraction, inflammations, immune responses, and long-term potentiation [3,4,10–18].

CaM consists of 148 residues and it has four special motifs called ‘EF-hand’; the EF-hand specifically interact with Ca²⁺. The reason is that the EF-hand sequence contains a highly conserved motif at the binding sites; the motif is the most common motif found in Ca²⁺-binding proteins [4,19–22]. The EF-hand motifs have been found in other Ca²⁺-binding proteins, such as Troponin C and Calbindin, and these proteins comprise a “EF-hand protein family” [19–21,23,24]. In the solution state, The EF-hand motif forms a helix-loop-helix structure [19,20,25–27]. The canonical EF-hand has the central loop consisting of

many glutamates and aspartates (negatively charged amino acids), and then these amino acids encourage the loop to capture Ca^{2+} ions [4,20,21].

Monomeric structures of both Ca^{2+} -bound CaM (holo-CaM) [28–37] and unbound CaM (apo-CaM) [38,39] have been studied experimentally. For example, X-ray crystallography and nuclear magnetic resonance (NMR) experiments have shown that CaM has two almost symmetrical globular domains; the domains are separated by a long linker region. The 1st and 2nd EF-hand are contained in the N-terminal domain (N-lobe), and the 3rd and 4th EF-hand are contained in the C-terminal domain (C-lobe). The structures of the N-, C-lobe, and linker region of apo-CaM are different from those of holo-CaM, indicating that CaM undergoes conformational change induced by Ca^{2+} -binding.

Both N- and C-lobe have four helices (the entering- and exiting-helix of two EF-hands). The NMR experiments have shown that the helices in apo-CaM form a single twisted four-helix-bundle. The linker region is disordered and flexibly connects the N-lobe and C-lobe, and then, the N- and C-lobe are expected to almost freely move independently from each other in the solution [38,39]. On the other hand, when Ca^{2+} binds, the EF-loop is pinched by Ca^{2+} and the interaction between the entering- and exiting-helix of each EF-hand is inhibited, causing the helices to separate each other [28,29,31–37]. This structural change exposes hydrophobic amino acids buried in the helix bundle, forming a hydrophobic pocket; the pocket is the binding site for the target protein [19,20]. The EF-hand conformations of holo-CaM and apo-CaM are referred to as “open conformation” and “closed conformation”, respectively. In the holo-CaM structure, the linker region is often a continuous helix and the whole structure is dumbbell-shaped.

Ca^{2+} -activated CaM regulates CaM-dependent proteins by forming a complex with them. Ordinary CaM-dependent proteins contain a CaM-binding domain (CaMBD), which is characterized by a high helix tendency and a net positive charge in the binding region. The structure of the CaM-CaMBD complex has been studied by X-ray crystallography and NMR experiments. For human CaM, the following complex structures with various proteins are known; CaM-dependent protein kinases (CaMK) [40,41], myosin light chain kinases (MLCK) [42–44], calcineurin (CN) [45–48], death-associated protein kinases (DAPK) [49,50], anthrax edema factor (EF) [51–54], and nitric oxide synthases (NOS) [55–58] have been deposited in the Protein Data Bank (PDB). In the canonical binding complex, the linker region is bent so that CaM wraps around CaMBD on the target protein. In 2013, Tidow et al. classified such canonical complexes with respect to their interaction patterns and reported conformational diversity of CaM-CaMBD complex [59].

In the field of biochemistry, a protein is often enhanced or reduced by an effector molecule that binds to a site distant from an active site [60,61]. Such phenomena are referred to as ‘allosteric regulation’ or ‘allostery’, and a molecule-enhancing activity is also called an ‘allosteric activator’, whereas a reducing one is called an ‘allosteric inhibitor’. In many proteins, the effector-induced signal propagation is closely associated with structural changes. The allostery is first attributed to the functional enhancement of hemoglobin in 1904, and today, the allostery is widely accepted as an essential mechanism of cellular processes [62,63]. For CaM, the Ca^{2+} -binding site is spatially too distant from the linker region to directly interact with each other. Then, the allosteric regulation is expected to mediate in order to propagate the Ca^{2+} -induced signal into an enzymatic activity. However, it is not yet clear how Ca^{2+} regulates the overall structure of CaM.

In 2008, Gsponer et al. reported structural ensembles representing the dynamics of CaM in a monomeric Ca^{2+} -bound state (PDB ID 2k0e) and in complex with MLCK (PDB ID 2k0f) [43]. The structures of 2k0e show large diffusion-like movement, as well as that of apo-CaM (PDB ID 1dmo [38]); it is in contrast to the holo-CaM structures determined by X-ray crystallography, such as PDB ID 1c1l [28] and 3c1n [29]. Their results indicated that Ca^{2+} -binding induces “population shift” through structural fluctuations, which gives rise to correlated motions. In our previous work, the structural ensemble reported by Gsponer (PDB ID 2k0e) was analyzed to identify the allosteric interactions [64].

Since the molecular dynamics (MD) simulation of CaM was performed by Komeiji et al. in 2002, many works employing the MD simulations have been made on CaM [65]. However, the SAXS experiment conducted in 2012 reported that the structural change of CaM takes from a millisecond to a second in a timescale [66]. The timescale currently affordable by ordinary MD simulation is a few hundred nanoseconds to microseconds, while the timescale of CaM is longer by more than 10^3 times. Useful but time-consuming calculations, such as the calculation of the free-energy landscape (FEL), for example, are not possible with the conventional MD simulations.

To overcome the time limitation, many simulation methods that facilitate effective sampling, have been proposed. For example, “umbrella sampling” that uses a harmonic potential or modified “flat-bottom” potential to facilitate an extensive sampling, is widely used [67–69]. Since the dimension of the conformation space is too large to sweep, collective variables, such as center-of-mass and RMSD, have been used to sweep multidimensional conformation space by lower dimensional sampling [70,71]. In our sampling, variables from principal component analysis (PCA) were used; the variables were chosen so that they were not affected by rotation and translation.

In a previous work, we proposed a method which combines an efficiency of a coarse-grained model (CGM) for conformational search and accuracy of an all-atom model (AAM) named multi-scale divide-and-conquer MD (MSDC-MD) [72] and demonstrated that the FEL of an intrinsically disordered protein, which is one of CaMBDs, could be evaluated correctly. In the present work, MSDC-MD was applied to the large conformational change of CaM by using the NMR experimental structures instead of CGM-MD-derived structures adopted before, and analyzed the FEL to obtain useful information for conformational change of CaM.

2. Materials and Methods

In our previous work [64], the monomeric CaM structural ensemble (PDB ID 2k0e) was analyzed by PCA. The first and second principal components corresponded to the relative domain motion (Figure 1a,b), and the cumulative proportion of the variance was about 80%. The distribution of monomeric structures on the plane by the first and second principal components had a horseshoe shape, as shown in Figure 1c (such distribution was also reported by Kurkcuglu et al. in 2016 [73]).

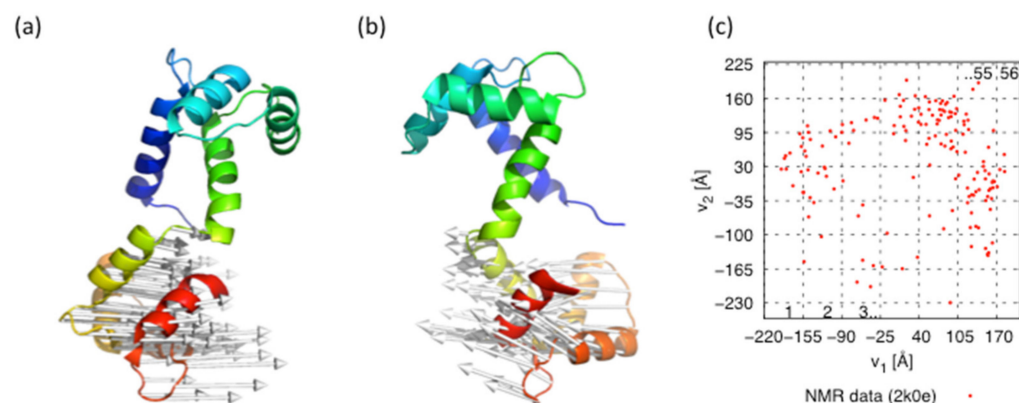


Figure 1. Porcupine plots of (a) the first eigenvector and (b) the second eigenvector mapped on the 20th model in NMR structures (PDB ID 2k0e). (c) Scatter plot of the NMR structures (PDB ID 2k0e). The x - and y -axis are the first and second principal component, respectively. The numbers of small areas are written sequentially.

The NMR structures (PDB ID 2k0e) were analyzed by the PCA to determine the reaction coordinate. Before PCA, to remove the effects of translation and rotation, root-mean-square-distance (RMSD) fitting with respect to the “reference coordinate” (first model’s N-lobe, C α positions 5-70; $s_\nu = (x_\nu, y_\nu, z_\nu)$ for $\nu = 5 \cdots 70$) was performed on the original C α position $r_i = (x_i, y_i, z_i)$,

$$r'_i = R(r_i - Q) \quad \text{for } i = 1 \cdots 148$$

$$Q = \frac{1}{66} \sum_{v=5}^{70} r_v$$

$$R = (A^t A)^{1/2} A^{-1}$$

where the vector Q is the centroid of the fitting $C\alpha$ atoms and the matrix R is a 3×3 rotational matrix. The rotational matrix R depends on r_v and s_v through the cross-covariance matrix A , defined as follows [74],

$$A_{ab} = \sum_{v=5}^{70} (r_{va} - Q_a)(s_{vb} - P_b) \quad \text{for } a, b = 1 \cdots 3$$

$$P = \frac{1}{66} \sum_{v=5}^{70} s_v$$

where the vector P is the centroid of the reference coordinate. Then, the fitted coordinate $X' = (r'_1, \cdots, r'_N)$ was analyzed by PCA to obtain the eigenvalues and eigenvectors ($N = 148$). The projection of the structure to n th principal component (v_n) can be written as $v_n = \sum_{k=1 \cdots 3N} c^{(n)}_k \cdot X'_k$ where $c^{(n)}$ is the n th eigenvector of a variance-covariance matrix $(\Lambda)_{kl} = \langle (X'_k - \langle X'_k \rangle) \cdot (X'_l - \langle X'_l \rangle) \rangle$ of X' ($\langle \cdots \rangle$ indicates an ensemble average, $k, l = 1 \cdots 3N$), which satisfies the following equation.

$$\Lambda c^{(n)} = \lambda_n \cdot c^{(n)}$$

In order to perform MSDC-MD, the monomeric structures on the v_1, v_2 -plane were divided into 56 small areas (Figures 1c and 2 dashed line), where the sizes of the small areas were chosen so that the following all-atom model (AAM) MD simulations can sweep the small area. Note here that this process is based on trial and error to date, because the way to know the optimum size of the area is unknown a priori. When the size is too large, individual AAM-MD cannot sweep the area, nevertheless, when the size is too small, the ergodicity might break down.

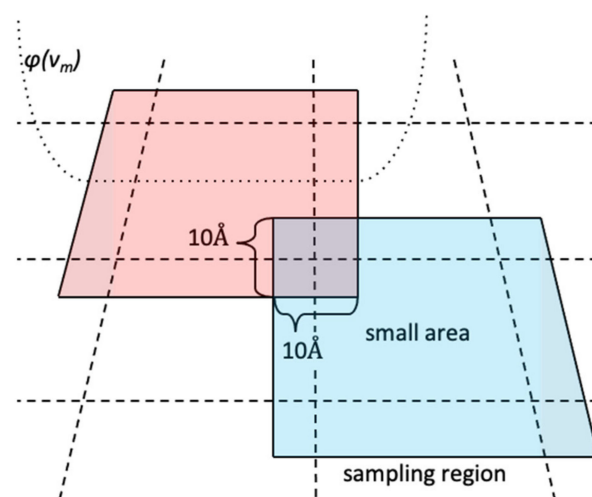


Figure 2. Graphical definition of the small area (dashed line), sampling region (solid line), and $\phi(v_m)$ (dotted line).

Multiple AAM-MD simulations were initiated at a randomly selected AAM structure using a modified version of GROMACS [75] (in a small area without the monomeric structure, AAM-MD simulation was not performed). To estimate the statistical error, this process was performed three times, changing the initial structure and the initial velocity. For the simulations, AMBER03 [76] force field was used for the protein and ions. Ca^{2+} parameter was $\sigma = 3.0524 \text{ \AA}$ and $\epsilon = 0.45962 \text{ kcal/mol}$ [77]. The periodic boundary condition

in that 20 Å buffer was taken from the most outer atom, was used and CaM was solvated in the TIP3P water models [78]. The numbers of water molecules were different for different initial structures, and then the total number of atoms varied from 52,754 to 68,597. The particle mesh Ewald method [79–81], with cutoff = 10 Å, was used for Coulomb interaction calculations. The total charge of the system was neutralized by adding Na⁺ ions. The Lennard-Jones potential, with cutoff = 14 Å, was used for van der Waals interactions. After energy minimizations and 1 ns of equilibration simulations with position restraints, 200 ns of multiple production simulations were performed independently, and for all AAM-MD simulations, the time step was 2 fs. The temperature and pressure of these simulations were maintained to be $T = 300$ K and $P = 1$ bar by the Berendsen thermostat [82] and Berendsen barostat [83], respectively. In the production runs, the following umbrella-like potential was imposed.

$$\phi(v_m) = \begin{cases} \frac{k}{2}(v_m^{\min} - v_m)^2 & \text{for } v_m < v_m^{\min} \\ 0 & \text{for } v_m^{\min} \leq v_m \leq v_m^{\max} \\ \frac{k}{2}(v_m - v_m^{\max})^2 & \text{for } v_m^{\max} < v_m \end{cases}$$

where $m = 1$ or 2 , the spring constant $k = 0.048$ kcal/mol/Å², v_m^{\min} and v_m^{\max} are the lower and upper limits of the sampling region, respectively. The difference between “small area” and “sampling region” is illustrated in Figure 2. The sampling regions overlap with the neighboring small areas by 5 Å. For example, the parameters of the sampling region 1 and 2 are taken to be $v_1^{\max(1)} - v_1^{\min(2)} = 10$ Å. Then, the relative weight of between the small area 1 and 2 can be written as $\omega_{12} = \log(N_2) - \log(N_1)$, where N_1 and N_2 are the number of the samples from the sampling region 1 and 2 in $v_1^{\min(2)} \leq v_1 \leq v_1^{\max(1)}$. In general, the relative weight between the small areas i and j can be written as $\omega_{ij} = \log(N_j) - \log(N_i)$, where N_i and N_j are the number of samples from the sampling region i and j in $v_m^{\min(j)} \leq v_m \leq v_m^{\max(i)}$. All structural samples in $v_m < v_m^{\min}$ or $v_m^{\max} < v_m$ were excluded from the FEL calculation. The entire weight over all sampling regions (W_i) is then obtained as follows.

$$W_j^{(c+1)} = \omega_{ij} + W_i^{(c)} \text{ for } N_i > 0 \text{ and } N_j > 0$$

where i, j are indexes of the sampling region, c is the iteration number and $W_v^{(0)} = 0$; the initial sampling region v is determined so that the number of overlapping regions is maximized, as, even if there is no overlap with the next region, the relative weight might be determined through the diagonally across region. Then, the above iteration was continued until all regions were linked. The entire FEL was obtained by summing the samples in the sampling region i with the final weight W_i as follows.

$$F(v_1, v_2) = k_B T \ln \left[\frac{\sum_{i=1}^{56} \exp(W_i) \left\{ \frac{\sum_t \delta(v_1(t)-v_1) \delta(v_2(t)-v_2) / M(v_1(t), v_2(t))}{L_i} \right\}}{\sum_{i=1}^{56} \exp(W_i) \left\{ \frac{\sum_t 1 / M(v_1(t), v_2(t))}{L_i} \right\}} \right]$$

where k_B is the Boltzmann constant, the index t and L_i are, respectively, the time step and the number of samples obtained from each sampling region i (please remember that samples out of the sampling region is excluded) and $M(v_1(t), v_2(t))$ is the number of overlapping; if $(v_1(t), v_2(t))$ is included in a region that is swept twice, $M = 2$. For this study, the difference of the entire FEL caused by the different choice of v was satisfactory smaller than the statistical error.

The force of $\phi(v_m)$ can be written as follows.

$$-\nabla\phi(v_m) = \begin{cases} k(v_m^{\min} - v_m) \nabla v_m & \text{for } v_m < v_m^{\min} \\ 0 & \text{for } v_m^{\min} \leq v_m \leq v_m^{\max} \\ k(v_m - v_m^{\max}) \nabla v_m & \text{for } v_m^{\max} < v_m \end{cases}$$

Since the vector Q and the rotation matrix R depend on original Cartesian coordinates $X_i = (r_1, \dots, r_N)$, ∇v_m can be written as follows.

$$\begin{aligned} \frac{\partial v_m}{\partial X_i} &= \sum_{j=1}^N \sum_{a=1}^3 c_{3j+k}^{(m)} \frac{\partial X'_{3j+a}}{\partial X_i} \\ &= \sum_{j=1}^N \sum_{a=1}^3 c_{3j+a}^{(m)} \left\{ \sum_{b=1}^3 \frac{\partial R_{ab}}{\partial X_i} \left(X_{3j+b} - Q_b \right) + R_{ab} \left(\delta_{i,3j+l} - Q_b \right) + R_{ab} \left(X_{3j+l} - \frac{\partial Q_b}{\partial X_i} \right) \right\} \end{aligned}$$

In order to show the efficiency of MSDC-MD's sampling, the non-arbitrary structure of a given area on FEL is shown as a "representative" structure. The representative structure was defined as a centroid in RMSD. Let Δ_{ij} be the RMSD of structure i with respect to structure j , then the total distance between an i and others are measured as $\Delta_i = \sum_{j \neq i} \Delta_{ij}$. Then, the representative structure was defined as that with the smallest Δ_i .

In our previous study [64], the allosteric interactions were identified as a contact probability. These interactions are also used to analyze the FEL. Suppose two residues, i and j , where a distance between any atom in residue i and another atom in residue j is less than 4.5 Å, the residues are identified as a contacting residue pair.

3. Results and Discussion

The entire FEL ($F(v_1, v_2)$, $T = 300$ K, $k_B T = 0.6$ kcal/mol) obtained by MSDC-MD is shown in Figure 3, which shows that the FEL has a complex multi-valley structure. The red points correspond to the NMR structures (Figure 3 red; PDB ID 2k0e), and it can be seen from Figure 3 that the distribution of the NMR structures roughly coincided with the basins of the FEL. The monomeric elongated structure (Figure 3 purple; PDB ID 1c1l) is located at the edge of a broad basin around $(v_1, v_2) = (50, 100)$. Notably, the ring-like structure in the complex (Figure 3 green; PDB ID 4q5u) was not located in a stable FEL's basin, but in a slightly higher free-energy (structurally unstable) region.

In order to confirm whether statistically sufficient samples were obtained or not, the RMSD, with respect to the elongated structure and the ring-like structure, were calculated (Figure 4a). It can be seen from the figure that the smallest C α -C α RMSD, with respect to the elongated structure and the ring-like structure, are, respectively, 2.7 Å and 2.8 Å. Considering that a C α distance between adjacent amino acids is about 3.8 Å, the MSDC-MD has succeeded in sampling structures similar enough to the elongated structure or the ring-like structure. Indeed, when the structures of the minimum RMSD and representative structures obtained from MSDC-MD are superimposed on the elongated structure and the ring-like structure, it can be seen that they coincided well with each other (Figure 4b–e); the RMSD of the representative structure around the elongated and ring-like structure, with respect to the elongated and ring-like structure, was, respectively, 3.2 Å and 2.8 Å. Then, it can be said that the shape of the FEL around the elongated structure and the ring-like structure in Figure 3 is not due to a sampling error. Since the elongated structure was obtained from X-ray crystallography, the location of the elongated structure is away from the region where many NMR structures are located, which would reflect differences in experimental conditions. On the other hand, the ring-like structure is probably intrinsically unstable, and it is one that can only be stabilized by forming a complex.

To validate the correctness of the FEL, the FEL obtained by 5 μ s conventional AAM-MD starting from an elongated structure is shown in Figure 5a. Further, the comparisons of one-dimensional FELs are shown in Figure 5b,c. The FEL shown in Figure 5b was obtained from averaging the two-dimensional FEL on the rectangle region from $(-210 \text{ \AA}, 110 \text{ \AA})$ to $(190 \text{ \AA}, 140 \text{ \AA})$ along the v_2 -axis (red rectangle in Figure 5a). Similarly, the FEL shown in Figure 5c was obtained from averaging the two-dimensional FEL on the rectangle region from $(170 \text{ \AA}, 0 \text{ \AA})$ to $(140 \text{ \AA}, 160 \text{ \AA})$ along the v_1 -axis (orange rectangle in Figure 5a). The position of the averaging area was shifted by $\pm 10 \text{ \AA}$, but the qualitative trend of the graph did not change.

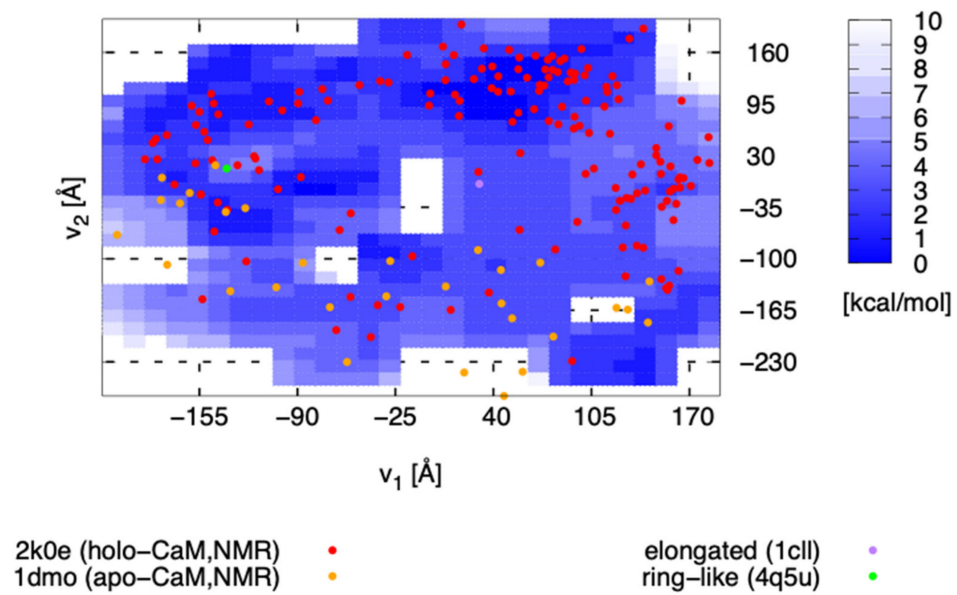


Figure 3. The entire free-energy landscape obtained from MSDC-MD. The x - and y -axis are respectively v_1 and v_2 . The red and orange points show the holo-NMR and apo-NMR structures (PDB ID 2k0e, 1dmo), respectively, the green and purple points, respectively, show the elongated structure (PDB ID 1c1l) and the ring-like structure (PDB ID 4q5u).

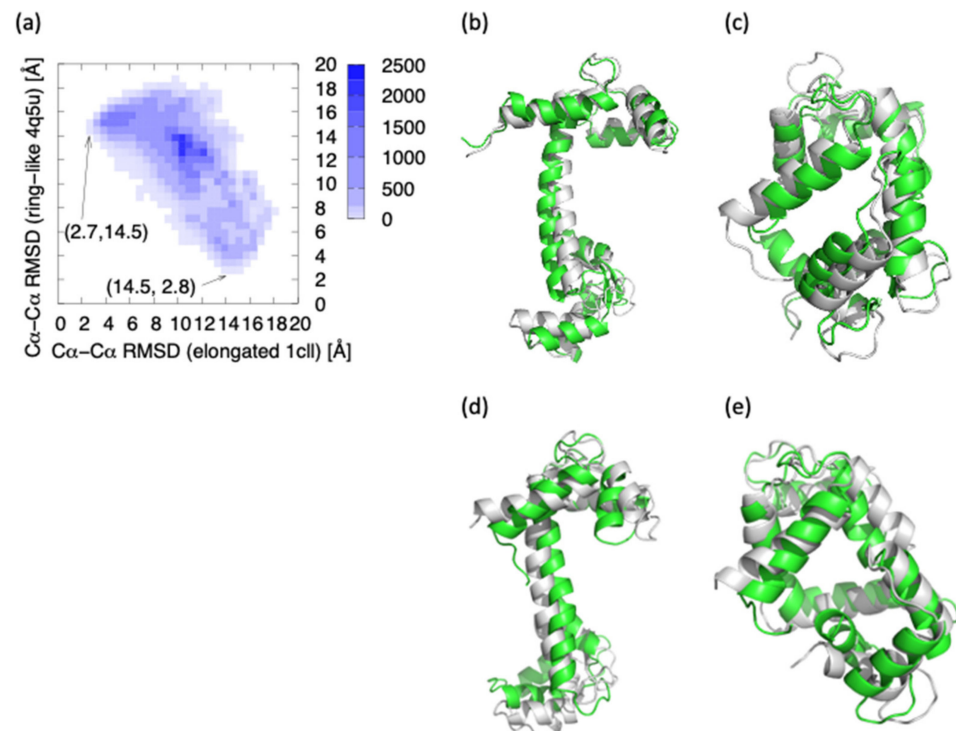


Figure 4. (a) The (unweighted) distribution of the structures obtained from MSDC-MD, as a function of $C\alpha$ - $C\alpha$ RMSD; the x - and y -axis are, respectively, $C\alpha$ - $C\alpha$ RMSD, with respect to the elongated structure (1c1l) and the ring-like structure (4q5u). The total number of the samples is 252,168. (b) The elongated structure (white) and the most similar structure to the elongated structure obtained from the MSDC-MD simulation (green). (c) The ring-like structure (white) and the most similar structure to the ring-like structure obtained from the MSDC-MD simulation (green). (d) The elongated structure (white) and the representative structure around the elongated structure ($20 \leq v_1 \leq 50$ and $-20 \leq v_2 \leq 10$, green, RMSD = 3.2 Å). (e) The ring-like structure (white) and the representative structure around the ring-like structure ($-150 \leq v_1 \leq -120$ and $0 \leq v_2 \leq 30$, green, RMSD = 2.8 Å).

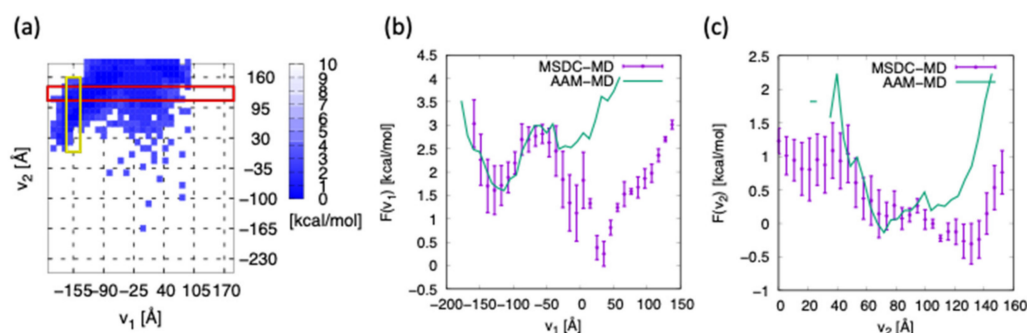


Figure 5. (a) FEL obtained from the conventional AAM-MD of 5 μ s initiated at the elongated structure. (b) One-dimensional FEL obtained from the red rectangle in (a) as a function of v_1 . (c) One-dimensional FEL obtained from the orange rectangle in (a) as a function of v_2 .

It can be seen from Figure 5b that both AAM-MD and MSDC-MD sampled from the left basin located around $v_1 = -130$ Å. The shape of FELs roughly coincided with each other only around the left basin. However, AAM-MD failed in sampling above $v_1 = -50$ Å, whereas MSDC-MD succeeded in finding a new basin around $v_1 = 50$ Å. This basin corresponds to the broad basin around $(v_1, v_2) = (50$ Å, 100 Å), as shown in Figure 3, but AAM-MD does not detect the basin, as shown in Figure 5a. Therefore the FEL of AAM-MD at the right basin is shallower than that of MSDC-MD. AAM-MD, as shown in Figure 5c, could only sample a range of 40 Å $< v_2 < 100$ Å, while MSDC-MD could sample a much wider range of 0 Å $< v_2 < 160$ Å.

In our previous study [64], in order to identify the allosteric interactions among holo-CaM, the holo-CaM NMR structures (PDB ID: 1dmo) were compared to the “chimera” structure; the chimera structure was made by combining the linker region of the apo-CaM structures and the N- and C-lobe of holo-elongated CaM (PDB ID: 1cll). From the study, the interactions that are included in the holo-CaM NMR structures, but not in the chimera structures, had been identified as the contact probability (Figure 6a). Presumably, these interactions include allosteric interactions.

In order to investigate the relationship between the inter-domain interactions and the positions on the FEL, the inter-domain interactions are divided into five groups (C1–C5; Figure 6a), and the structures that have C1–C5 interactions were marked on the FEL (Figure 6b). As shown in Figure 6b, the structures forming C1–5 are projected following their own patterns instead of being projected randomly, indicating that the C1–5 interactions play essential roles in regulating the inter-domain motion. From Figure 6b, most NMR data are distributed (i) in the region around $(v_1, v_2) = (-140, 50)$, (ii) the region around $(50, 90)$ and (iii) the region around $(140, -30)$. Similarly, the FEL basins are in (i), (ii) and (iii), where the lowest point of the FEL is included in (ii), and the C3, C4 forming structures are populated. On the other hand, (iv) region $(20 < v_1 < 70, -200 < v_2 < 50)$ is a broad and stable region, and the elongated structures are included here.

Since the distribution of NMR data of apo-CaM is basically distributed on the lower part of the FEL, the process of the initial structural change from apo-CaM to holo-CaM would correspond to the path on the FEL from the lower to the most stable point in (ii). The most probable path, in this regard, is the one passing through the region (iv). The reason why the experimentally famous elongated structure is actually included in this region may be the result of X-ray crystallography capturing the structural change from apo-CaM to holo-CaM upon Ca^{2+} binding. Since the lowest point of the FEL is located at point (ii), the ring-like structure is not the most stable state for monomeric holo-CaM. However, the FEL basin around the ring-like structure indicates that even the monomeric holo-CaM has interactions (C4, C5) to form the ring-like structure. Around the (iii) region, inter-domain interactions (C1, C2) are formed, but as the FEL barrier exits between region (ii) and (iii), as shown in the subset of Figure 6b, the difference of the relative free-energy to region (iii) ($\Delta\Delta F$), between region (iii) and the saddle point of the barrier, is 1.5 kcal/mol, and $\Delta\Delta F$

between the saddle point and region (ii) is 4.5 kcal/mol. On the other hand, no clear barrier was found between region (iii) and (iv). Therefore, the structures that once went to region (iii) would back region (iv) against the barrier, while the inter-domain interactions formed in region (iii) are dissociated, in order to take an elongated structure. Then, if mutations that decrease the FEL barrier are generated, the mutated CaM may change its structure in a shorter time.

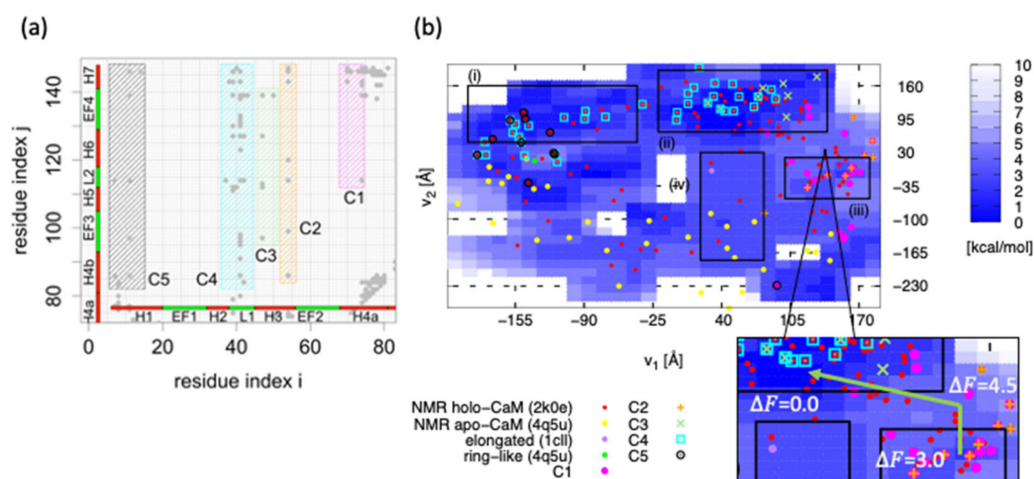


Figure 6. (a) The inter-domain contact probabilities whose contact ratio in holo-CaM is larger than that of chimera structures. The interactions can be divided into five groups (C1–C5). (b) The entire free-energy landscape obtained from MSDC-MD. The x- and y-axis are, respectively, v_1 and v_2 . The red points show the NMR structures (PDB ID 2k0e), the orange points show the apo-NMR structure (1dmo), and the green and purple points, respectively, show the elongated structure (PDB ID 1c1l) and the ring-like structure (PDB ID 4q5u). C1–C5 forming structures are, respectively, indicated as the pink point, orange cross, green cross, cyan square, and black circle. In the subset, the free-energy values relative to the region (iii) are shown in kilocalories per mole.

However, based on the amount of NMR data and the distribution of FELs, it is reasonable to assume that the structural changes occur in the order (iv), (ii), and (i) at this stage. Although the structural change of the individual AAM-MDs in the MSDC-MD is virtual behavior under fictitious confinement potentials, the overall FEL can be quickly calculated by reweighting the individual free energies. In this case, we compared the FEL of 200 ns MSDC-MD with that of the 5 μ s, and the 200 ns MSDC-MD was able to calculate the FEL that is clearly broader and consistent with the NMR structure distribution. Furthermore, since the AAM-MDs in the MSDC-MD do not need to communicate with each other, it is very compatible with parallel computing. We can then conclude that the MSDC-MD is an excellent method for FEL analyses in recent situations where parallel computing is commonly used.

4. Conclusions

In our study, we applied a multi-scale simulation method that divides the conformation space into small areas to enable us to perform a well-equilibrated MD simulation, named ‘MSDC-MD’, to the free-energy analysis of CaM. In order to investigate the efficiency and accuracy, MSDC-MD simulation of CaM was performed. Since Komeiji et al. in 2002, CaM has been a good example to demonstrate the computational method, because it exhibits large conformational changes including domain rotation and translation in the Ca^{2+} -signal transduction process. As the process takes nearly 1 ms, conventional MD simulations have failed to sufficiently sample wide conformational regions of CaM.

MSDC-MD succeeded in providing the overall conformational change of the CaM on the FEL yield by v_1 and v_2 ; the conformational samples obtained from MSDC-MD sufficiently covered the NMR and X-ray crystal structures indicating the efficiency of MSDC-MD.

Furthermore, the MSDC-MD structures include samples similar to the famous elongated structure (PDB ID 1c1l, RMSD = 2.8 Å at minimum) and ring-like structure (PDB ID 4q5u, RMSD = 2.7 Å at minimum), as shown in Figure 2. As the C α -C α distance connected by covalent bonds is about 3.8 Å, we conclude that the MSDC-MD succeeded in sampling the important structures, even though we started the simulations at different conformations.

The accuracy of the MSDC-MD was also investigated by comparing the FELs obtained by MSDC-MD and the conventional MD. Although a long ordinary MD simulation of 5 μ s was performed, the conventional MD only gave left-upper region of FEL on the v_1 , v_2 space. Then, one-dimensional FEL was calculated to compare the shape of FELs. The FEL obtained by the conventional MD on v_1 detected only the left basin, and it was trapped there until the end of the MD simulation. On the other hand, MSDC-MD can detect not only the left basin, but also another basin that is much deeper than the left one. Compared with the shape of the left basin, the shapes coincided with each other within the statistical error, which indicates that the MSDC-MD sufficiently reproduces the same entire FEL as the ordinary MD simulation, if the ordinary MD simulations of the millisecond time scale could be performed. The comparison of FEL on v_2 also demonstrated that the shape of FELs coincided with each other within the statistical error at the bottom of the ordinary MD's FEL.

The FEL analysis provided the picture of how conformational changes occur on the FEL, and the important interactions on each stage of conformational change (C1–5) were linked to the FEL. The interactions C1–5 were defined to analyze the NMR structures in our previous study [64]. From the distribution of the NMR structures only, one might think that conformational change would occur along a path (iii) \rightarrow (ii) \rightarrow (i) on the upper region. However, the MSDC-MD's FEL shows that the free-energy barrier between region (ii) and (iii), leads to the structures in region (iii) going back to region (iv). From the viewpoint of interactions, interactions C1–2 formed in region (iii) would be dissociated to form the elongated structure. Then, the process of conformational change on the FEL would occur along a path (iv) \rightarrow (ii) \rightarrow (i) when CaMBD is present. Such detailed information could not only be obtained from the experimental data, and the FEL analysis is necessary to complement the experimental data and investigate the biomolecular system more deeply.

Author Contributions: Conceptualization, H.S.; methodology, H.S.; software, H.S.; validation, H.S. and Y.S.; formal analysis, H.S.; investigation, H.S.; resources, H.S.; data curation, H.S.; writing—original draft preparation, H.S.; writing—review and editing, Y.S.; visualization, H.S.; supervision, H.S.; project administration, Y.S.; funding acquisition, Y.S. All authors have read and agreed to the published version of the manuscript.

Funding: This work was partially supported by grant-in-aid for the innovative research “Hydrogeomics” and “Biometal Sciences” (Grant Numbers 19H05047 and 20H05497) by the Ministry of Education, Culture, Sports, Science and Technology (MEXT), Japan and by JST CREST, Japan (No. JP20338388 (Y.S.)). This work was partially supported by MEXT Quantum Leap Flagship Program (MEXT Q-LEAP, Grant Number JPMXS0120330644).

Institutional Review Board Statement: Not applicable.

Informed Consent Statement: Not applicable.

Data Availability Statement: The data presented in this study are available on request from the corresponding author.

Acknowledgments: In this study, all structural figures were created by PyMOL [84], and some structural analyses were performed by statistical computing and graphic package ‘R’ [85]. This research, in part, used computational resources of Oakforest-PACS and Cygnus provided by the Multidisciplinary Cooperative Research Program in the Center for Computational Sciences, University of Tsukuba.

Conflicts of Interest: The authors declare no conflict of interest.

References

1. Putney, J.W. Calcium signaling. *Cell* **2005**, *80*, 1–540.
2. Berridge, M.J.; Bootman, M.D.; Lipp, P. Calcium—A life and death signal. *Nature* **1998**, *395*, 645–648. [[CrossRef](#)] [[PubMed](#)]
3. Chin, D.; Means, A.R. Calmodulin: A prototypical calcium sensor. *Trends Cell Biol.* **2000**, *10*, 322–328. [[CrossRef](#)]
4. Gifford, J.; Walsh, M.; Vogel, H. Structures and metal-ion-binding properties of the Ca²⁺-binding helix-loop-helix EF-hand motifs. *Biochem. J.* **2007**, *405*, 199–221. [[CrossRef](#)]
5. Klee, C.B.; Vanaman, T.C. Calmodulin. *Adv. Protein Chem.* **1982**, *35*, 213–321. [[PubMed](#)]
6. Kakiuchi, S.; Yamazaki, R. Calcium dependent phosphodiesterase activity and its activating factor (PAF) from brain. Studies on cyclic 3',5'-nucleotide phosphodiesterase (III). *Biochem. Biophys. Res. Commun.* **1970**, *41*, 1104–1110. [[CrossRef](#)]
7. Cheung, W.Y. Cyclic 3',5'-nucleotide phosphodiesterase. Demonstration of an activator. *Biochem. Biophys. Res. Commun.* **1970**, *38*, 533–538. [[CrossRef](#)]
8. Teo, T.S.; Wang, T.H.; Wang, J.H. Purification and properties of the protein activator of bovine heart cyclic adenosine 3',5'-monophosphate phosphodiesterase. *J. Biol. Chem.* **1973**, *248*, 588–595. [[CrossRef](#)]
9. Teo, T.S.; Wang, J.H. Mechanism of activation of a cyclic adenosine 3':5' monophosphate phosphodiesterase from bovine heart by calcium ions. Identification of the protein activator as a Ca²⁺ binding protein. *J. Biol. Chem.* **1973**, *248*, 5950–5955. [[CrossRef](#)]
10. Kumar, V.; Chichili, V.; Zhong, L. Structural basis for the interaction of unstructured neuron specific substrates neuromodulin and neurogranin with calmodulin. *Sci. Rep.* **2013**, *3*, 1392. [[CrossRef](#)] [[PubMed](#)]
11. Tansey, M.G.; Luby-Phelps, K.; Kamm, K.E.; Stull, J.T. Ca²⁺-dependent phosphorylation of myosin light chain kinase decreases the Ca²⁺ sensitivity of light chain phosphorylation within smooth muscle cells. *J. Biol. Chem.* **1994**, *269*, 9912–9920. [[CrossRef](#)]
12. Means, A.R.; Chafouleas, J.G. Calmodulin is involved in the regulation of cell proliferation. *Cell Biol. Int. Rep.* **1983**, *7*, 481–482. [[CrossRef](#)]
13. Kawai, T.; Nomura, F.; Katsuaki, H.; Copeland, N.G.; Gilbert, D.J.; Jenkins, N.A.; Shizuo, A. Death-associated protein kinase 2 is a new calcium/calmodulin-dependent protein kinase that signals apoptosis through its catalytic activity. *Oncogene* **1999**, *18*, 3471–3480. [[CrossRef](#)] [[PubMed](#)]
14. Fladmark, K.E.; Fladmark, K.E.; Brustugun, O.T.; Mellgren, G.; Krakstad, C.; Bøe, R.; Vintermyr, O.K.; Schulman, H.; Døskeland, S.O. Ca²⁺/calmodulin-dependent protein kinase II is required for microcystin-induced apoptosis. *J. Biol. Chem.* **2002**, *277*, 2804–2811. [[CrossRef](#)]
15. Racioppi, L.; Means, A.R. Calcium/calmodulin-dependent kinase IV in immune and inflammatory responses: Novel routes for an ancient traveller. *Trends Immunol.* **2008**, *29*, 600–607. [[CrossRef](#)] [[PubMed](#)]
16. Curtis, J.; Finkbeiner, S. Sending signals from the synapse to the nucleus: Possible roles for CaMK, Ras/ERK, and SAPK pathways in the regulation of synaptic plasticity and neuronal growth. *J. Neurosci. Res.* **1999**, *58*, 88–95. [[CrossRef](#)]
17. Prichard, L.; Deloulme, J.C.; Storm, D.R. Interactions between neurogranin and calmodulin in vivo. *J. Biol. Chem.* **1999**, *274*, 7689–7694. [[CrossRef](#)]
18. Soderling, T.R. CaM-kinases: Modulators of synaptic plasticity. *Curr. Opin. Neurobiol.* **2000**, *10*, 375–380. [[CrossRef](#)]
19. Ikura, M. Calcium binding and conformational response in EF-hand proteins. *Trends Biochem. Sci.* **1996**, *21*, 14–17. [[CrossRef](#)]
20. Grabarek, Z. Structural Basis for Diversity of the EF-hand Calcium-binding Proteins. *J. Mol. Biol.* **2006**, *359*, 509–525. [[CrossRef](#)]
21. Zhou, Y.; Yang, W.; Kirberger, M.; Lee, H.W.; Ayalasomayajula, G.; Yang, J.J. Prediction of EF-hand calcium-binding proteins and analysis of bacterial EF-hand proteins. *Proteins Struct. Funct. Genet.* **2006**, *65*, 643–655. [[CrossRef](#)] [[PubMed](#)]
22. Lewit-Bentley, A.; Réty, S. EF-hand calcium-binding proteins. *Curr. Opin. Struct. Biol.* **2000**, *10*, 637–643. [[CrossRef](#)]
23. Kawasaki, H.; Nakayama, S.; Kretsinger, R.H. Classification and evolution of EF-hand proteins. *BioMetals* **1998**, *11*, 277–295. [[CrossRef](#)]
24. Ravasi, T.; Hsu, K.; Goyette, J.; Schroder, K.; Yang, Z.; Rahimi, F.; Miranda, L.P.; Alewood, P.F.; Hume, D.A.; Geczy, C. Probing the S100 protein family through genomic and functional analysis. *Genomics* **2004**, *84*, 10–22. [[CrossRef](#)] [[PubMed](#)]
25. McPhalen, C.A.; Strynadka, N.C.J.; James, M.N.G. Calcium-Binding Sites in Proteins: A Structural Perspective. *Adv. Protein Chem.* **1991**, *42*, 77–82. [[PubMed](#)]
26. Nelson, M.R.; Chazin, W.J. Structures of EF-hand Ca²⁺-binding proteins: Diversity in the organization, packing and response to Ca²⁺ binding. *Biomaterials* **1998**, *11*, 297–318. [[CrossRef](#)]
27. Strynadka, N.C.J.; James, M.N.G. Crystal structures of the helix-loop-helix calcium-binding proteins. *Annu. Rev. Biochem.* **1989**, *58*, 951–999. [[CrossRef](#)]
28. Chattopadhyaya, R.; Meador, W.E.; Means, A.R.; Quijcho, F.A. Calmodulin structure refined at 1.7 Å resolution. *J. Mol. Biol.* **1992**, *228*, 1177–1192. [[CrossRef](#)]
29. Babu, Y.S.; Bugg, C.E.; Cook, W.J. Structure of calmodulin refined at 2.2 Å resolution. *J. Mol. Biol.* **1988**, *204*, 191–204. [[CrossRef](#)]
30. Taylor, D.A.; Sack, J.S.; Maune, J.F.; Beckingham, K.; Quijcho, F.A. Structure of a recombinant calmodulin from *Drosophila melanogaster* refined at 2.2 Å resolution. *J. Biol. Chem.* **1991**, *266*, 21375–21380. [[CrossRef](#)]
31. Rao, S.T.; Wu, S.; Satyshur, K.A.; Sundaralingam, M.; Ling, K.Y.; Kung, C. Structure of *Paramecium tetraurelia* calmodulin at 1.8 Å resolution. *Protein Sci.* **1993**, *2*, 436–447. [[CrossRef](#)]
32. Ban, C.; Ramakrishnan, B.; Ling, K.Y.; Ching, K.; Sundaralingam, M. Structure of the recombinant *Paramecium tetraurelia* calmodulin at 1.68 Angstroms resolution. *Acta Crystallogr. Sect. D Biol. Crystallogr.* **1994**, *50*, 50–63. [[CrossRef](#)] [[PubMed](#)]

33. Rupp, B.; Marshak, D.R.; Parkin, S. Crystallization and preliminary X-ray analysis of two new crystal forms of calmodulin. *Acta Crystallogr. Sect. D Biol. Crystallogr.* **1996**, *52*, 411–413. [[CrossRef](#)] [[PubMed](#)]
34. Wilson, M.A.; Brunger, A.T. The 1.0 Å crystal structure of Ca²⁺-bound calmodulin: An analysis of disorder and implications for functionally relevant plasticity. *J. Mol. Biol.* **2000**, *301*, 1237–1256. [[CrossRef](#)] [[PubMed](#)]
35. Yun, C.H.; Bai, J.; Sun, D.Y.; Cui, D.F.; Chang, W.R.; Liang, D.C. Structure of potato calmodulin PCM6: The first report of the three-dimensional structure of a plant calmodulin. *Acta Crystallogr. Sect. D Biol. Crystallogr.* **2004**, *60*, 1214–1219. [[CrossRef](#)]
36. Lin, J.; van den Bedem, H.; Brunger, A.T.; Wilson, M.A. Atomic resolution experimental phase information reveals extensive disorder and bound 2-methyl-2,4-pentanediol in Ca²⁺-calmodulin. *Acta Crystallogr. Sect. D Struct. Biol.* **2016**, *72*, 83–92. [[CrossRef](#)]
37. Kumar, S.; Mazumder, M.; Gupta, N.; Chattopadhyay, S.; Gourinath, S. Crystal structure of Arabidopsis thaliana calmodulin7 and insight into its mode of DNA binding. *FEBS Lett.* **2016**, *590*, 3029–3039. [[CrossRef](#)]
38. Zhang, M.; Tanaka, T.; Ikura, M. Calcium-induced conformational transition revealed by the solution structure of apo calmodulin. *Nat. Struct. Biol.* **1995**, *2*, 758–767. [[CrossRef](#)]
39. Ishida, H.; Nakashima, K.; Kumaki, Y.; Nakata, M.; Hikichi, K.; Yazawa, M. The solution structure of apocalmodulin from *Saccharomyces cerevisiae* implies a mechanism for its unique Ca²⁺ binding property. *Biochemistry* **2002**, *41*, 15536–15542. [[CrossRef](#)]
40. Rellos, P.; Pike, A.C.W.; Niesen, F.H.; Salah, E.; Lee, W.H.; von Delft, F.; Knapp, S. Structure of the CaMKIIδ/calmodulin complex reveals the molecular mechanism of CamKII kinase activation. *PLoS Biol.* **2010**, *8*, e1000426. [[CrossRef](#)]
41. Gifford, J.L.; Ishida, H.; Vogel, H.J. Fast methionine-based solution structure determination of calcium-calmodulin complexes. *J. Biomol. NMR* **2011**, *50*, 71–81. [[CrossRef](#)] [[PubMed](#)]
42. Meador, W.E.; Means, A.R.; Quijcho, F.A. Target enzyme recognition by calmodulin: 2.4 Å structure of a calmodulin-peptide complex. *Science* **1992**, *257*, 1251–1255. [[CrossRef](#)] [[PubMed](#)]
43. Gsponer, J.; Christodoulou, J.; Cavalli, A.; Bui, J.M.; Richter, B.; Dobson, C.M.; Vendruscolo, M. A Coupled Equilibrium Shift Mechanism in Calmodulin-Mediated Signal Transduction. *Structure* **2008**, *16*, 736–746. [[CrossRef](#)] [[PubMed](#)]
44. Grishaev, A.; Anthis, N.J.; Clore, G.M. Contrast-matched small-angle x-ray scattering from a heavy-atom-labeled protein in structure determination: Application to a lead-substituted calmodulin-peptide complex. *J. Am. Chem. Soc.* **2012**, *134*, 14686–14689. [[CrossRef](#)]
45. Ye, Q.; Wang, H.; Zheng, J.; Wei, Q.; Jia, Z. The complex structure of calmodulin bound to a calcineurin peptide. *Proteins Struct. Funct. Genet.* **2008**, *73*, 19–27. [[CrossRef](#)] [[PubMed](#)]
46. Majava, V.; Kursula, P. Domain swapping and different oligomeric states for the complex between calmodulin and the calmodulin-binding domain of calcineurin A. *PLoS ONE* **2009**, *4*, e5402. [[CrossRef](#)]
47. Fallon, J.L.; Baker, M.R.; Xiong, L.; Loy, R.E.; Yang, G.; Dirksen, R.T.; Hamilton, S.L.; Quijcho, F.A. Crystal structure of dimeric cardiac L-type calcium channel regulatory domains bridged by Ca²⁺-calmodulins. *Proc. Natl. Acad. Sci. USA* **2009**, *106*, 5135–5140. [[CrossRef](#)]
48. Dunlap, T.B.; Guo, H.F.; Cook, E.C.; Holbrook, E.; Rumi-Masante, J.; Lester, T.E.; Colbert, C.L.; Vander, K.; Craig, W.; Creamer, T.P. Stoichiometry of the Calcineurin Regulatory Domain–Calmodulin Complex. *Biochemistry* **2014**, *53*, 5779–5790. [[CrossRef](#)]
49. De Diego, I.; Kuper, J.; Bakalova, N.; Kursula, P.; Wilmanns, M. Molecular basis of the death-associated protein kinase-calcium/calmodulin regulator complex. *Sci. Signal.* **2010**, *3*, ra6. [[CrossRef](#)]
50. Bertini, I.; Kursula, P.; Luchinat, C.; Parigi, G.; Vahokoski, J.; Wilmanns, M.; Yuan, J. Accurate solution structures of proteins from X-ray data and a minimal set of NMR Data: Calmodulin-peptide complexes as examples. *J. Am. Chem. Soc.* **2009**, *131*, 5134–5144. [[CrossRef](#)]
51. Shen, Y.; Lee, Y.S.; Soelaiman, S.; Bergson, P.; Lu, D.; Chen, A.; Beckingham, K.; Grabarek, Z.; Mrksich, M.; Tang, W.J. Physiological calcium concentrations regulate calmodulin binding and catalysis of adenylyl cyclase exotoxins. *EMBO J.* **2002**, *21*, 6721–6732. [[CrossRef](#)]
52. Shen, Y.; Guo, Q.; Zhukovskaya, N.L.; Drum, C.L.; Bohm, A.; Tang, W.J. Structure of anthrax edema factor-calmodulin-adenosine 5′-(α, β-methylene)-triphosphate complex reveals an alternative mode of ATP binding to the catalytic site. *Biochem. Biophys. Res. Commun.* **2004**, *317*, 309–314. [[CrossRef](#)] [[PubMed](#)]
53. Guo, Q.; Shen, Y.; Zhukovskaya, N.L.; Florián, J.; Tang, W.J. Structural and kinetic analyses of the interaction of anthrax adenylyl cyclase toxin with reaction products cAMP and pyrophosphate. *J. Biol. Chem.* **2004**, *279*, 29427–29435. [[CrossRef](#)] [[PubMed](#)]
54. Shen, Y.; Zhukovskaya, N.L.; Guo, Q.; Florián, J.; Tang, W.J. Calcium-independent calmodulin binding and two-metal-ion catalytic mechanism of anthrax edema factor. *EMBO J.* **2005**, *24*, 929–941. [[CrossRef](#)] [[PubMed](#)]
55. Xia, C.; Misra, I.; Iyanagi, T.; Kim, J.J.P. Regulation of interdomain interactions by calmodulin in inducible nitric-oxide synthase. *J. Biol. Chem.* **2009**, *284*, 30708–30717. [[CrossRef](#)]
56. Piazza, M.; Futrega, K.; Spratt, D.E.; Dieckmann, T.; Guillemette, J.G. Structure and dynamics of calmodulin (CaM) bound to nitric oxide synthase peptides: Effects of a phosphomimetic CaM mutation. *Biochemistry* **2012**, *51*, 3651–3661. [[CrossRef](#)]
57. Piazza, M.; Taiakina, V.; Guillemette, S.R.; Guillemette, J.G.; Dieckmann, T. Solution structure of calmodulin bound to the target peptide of endothelial nitric oxide synthase phosphorylated at Thr495. *Biochemistry* **2014**, *53*, 1241–1249. [[CrossRef](#)]
58. Piazza, M.; Dieckmann, T.; Guillemette, J.G. Structural Studies of a Complex between Endothelial Nitric Oxide Synthase and Calmodulin at Physiological Calcium Concentration. *Biochemistry* **2016**, *55*, 5962–5971. [[CrossRef](#)]
59. Tidow, H.; Nissen, P. Structural diversity of calmodulin binding to its target sites. *FEBS J.* **2013**, *280*, 5551–5565. [[CrossRef](#)]

60. Kern, D.; Zuiderweg, E.R.P. The role of dynamics in allosteric regulation. *Curr. Opin. Struct. Biol.* **2003**, *13*, 748–757. [[CrossRef](#)]
61. Swain, J.F.; Gierasch, L.M. The changing landscape of protein allostery. *Curr. Opin. Struct. Biol.* **2006**, *16*, 102–108. [[CrossRef](#)] [[PubMed](#)]
62. Bohr, C.; Hasselbalch, K.; Krogh, A. Ueber einen in biologischer Beziehung wichtigen Einfluss, den die Kohlensäurespannung des Blutes auf dessen Sauerstoffbindung übt. *Skand. Arch. Physiol.* **1904**, *16*, 402–412. [[CrossRef](#)]
63. Liu, J.; Nussinov, R. Allostery: An Overview of Its History, Concepts, Methods, and Applications. *PLoS Comput. Biol.* **2016**, *12*, e1004966. [[CrossRef](#)] [[PubMed](#)]
64. Shimoyama, H. A Structural Comparison of ‘Real’ and ‘Model’ Calmodulin Clarified Allosteric Interactions Regulating Domain Motion. *J. Biomol. Struct. Dyn.* **2018**, *37*, 1567–1581. [[CrossRef](#)] [[PubMed](#)]
65. Komeiji, Y.; Ueno, Y.; Uebayasi, M. Molecular dynamics simulations revealed Ca²⁺-dependent conformational change of Calmodulin. *FEBS Lett.* **2002**, *521*, 133–139. [[CrossRef](#)]
66. Yamada, Y.; Matsuo, T.; Iwamoto, H.; Yagi, N. A compact intermediate state of calmodulin in the process of target binding. *Biochemistry* **2012**, *51*, 3963–3970. [[CrossRef](#)]
67. Torrie, G.M.; Valleau, J.P. Nonphysical sampling distributions in Monte Carlo free-energy estimation: Umbrella sampling. *J. Comput. Phys.* **1977**, *23*, 187–199. [[CrossRef](#)]
68. Pai-Chi, L.; Miyashita, N.; Im, W.; Ishido, S.; Sugita, Y. Multidimensional umbrella sampling and replica-exchange molecular dynamics simulations for structure prediction of transmembrane helix dimers. *J. Comput. Chem.* **2013**, *35*, 300–308.
69. Leitgeb, M.; Schröder, C.; Boresch, S. Alchemical free energy calculations and multiple conformational substates. *J. Chem. Phys.* **2005**, *122*, 084109. [[CrossRef](#)]
70. Wojtas-Niziurski, W.; Meng, Y.; Roux, B.; Berneche, S. Self-Learning Adaptive Umbrella Sampling Method for the Determination of Free Energy Landscapes in Multiple Dimensions. *J. Chem. Theory Comput.* **2013**, *9*, 1885–1895. [[CrossRef](#)]
71. Wang, J.; Shao, Q.; Xu, Z.; Liu, Y.; Yang, Z.; Cossins, B.P.; Jiang, H.; Chen, K.; Shi, J.; Zhu, W. Exploring transition pathway and free-energy profile of large-scale protein conformational change by combining normal mode analysis and umbrella sampling molecular dynamics. *J. Phys. Chem. B* **2014**, *118*, 134–143. [[CrossRef](#)]
72. Shimoyama, H.; Yonezawa, Y. Atomistic detailed free-energy landscape of intrinsically disordered protein studied by multi-scale divide-and-conquer molecular dynamics simulation. *J. Comput. Chem.* **2021**, *42*, 19–26. [[CrossRef](#)] [[PubMed](#)]
73. Kurkcuoglu, Z.; Bahar, I.; Doruker, P. ClustENM: ENM-Based Sampling of Essential Conformational Space at Full Atomic Resolution. *J. Chem. Theory Comput.* **2016**, *12*, 4549–4562. [[CrossRef](#)] [[PubMed](#)]
74. Kabsch, W. A solution for the best rotation to relate two sets of vectors. *Acta Crystallogr. Sect. A Cryst. Phys. Diffr. Theor. Gen. Crystallogr.* **1976**, *32*, 922–923. [[CrossRef](#)]
75. Pronk, S.; Páll, S.; Schulz, R.; Larsson, P.; Bjelkmar, P.; Apostolov, R.; Shirts, M.R.; Smith, J.C.; Kasson, P.M.; van Der Spoel, D.; et al. GROMACS 4.5: A high-throughput and highly parallel open-source molecular simulation toolkit. *Bioinformatics* **2013**, *29*, 845–854. [[CrossRef](#)]
76. Duan, Y.; Wu, C.; Chowdhury, S.; Lee, M.C.; Xiong, G.; Zhang, W.; Yang, R.; Cieplak, P.; Luo, R.; Lee, T.; et al. A Point-Charge Force Field for Molecular Mechanics Simulations of Proteins Based on Condensed-Phase Quantum Mechanical Calculations. *J. Comput. Chem.* **2003**, *24*, 1999–2012. [[CrossRef](#)]
77. Shimoyama, H.; Shitaka-Takeda, M. Residue-residue interactions regulating the Ca²⁺-induced EF-hand conformation changes in calmodulin. *J. Biochem.* **2017**, *162*, 259–270. [[CrossRef](#)] [[PubMed](#)]
78. Jorgensen, W.L.; Chandrasekhar, J.; Madura, J.D.; Impey, R.W.; Klein, M.L. Comparison of simple potential functions for simulating liquid water. *J. Chem. Phys.* **1983**, *79*, 926–935. [[CrossRef](#)]
79. Darden, T.; York, D.; Pedersen, L. Particle mesh Ewald: An N·log(N) method for Ewald sums in large systems. *J. Chem. Phys.* **1993**, *98*, 10089–10092. [[CrossRef](#)]
80. Essmann, U.; Perera, L.; Berkowitz, M.L.; Darden, T.; Lee, H.; Pedersen, L.G. A smooth particle mesh Ewald method. *J. Chem. Phys.* **1995**, *103*, 8577–8593. [[CrossRef](#)]
81. Cheatham, T.E.; Miller, J.L.; Fox, T.; Darden, T.A.; Kollman, P.A. Molecular Dynamics Simulations on Solvated Biomolecular Systems: The Particle Mesh Ewald Method Leads to Stable Trajectories of DNA, RNA, and Proteins. *J. Am. Chem. Soc.* **1995**, *117*, 4193–4194. [[CrossRef](#)]
82. Berendsen, H.J.C.; Postma, J.P.M.; van Gunsteren, W.F.; Dinola, A.; Haak, J.R. Molecular dynamics with coupling to an external bath. *J. Chem. Phys.* **1984**, *81*, 3684–3690. [[CrossRef](#)]
83. Van Gunsteren, W.F.; Berendsen, H.J.C. Computer Simulation of Molecular Dynamics: Methodology, Applications, and Perspectives in Chemistry. *Angew. Chemie Int. Ed.* **1990**, *29*, 992–1023. [[CrossRef](#)]
84. DeLano, W. PyMOL. 2020. Available online: <http://www.pymol.org/pymol> (accessed on 30 September 2021).
85. R Development Core Team 3.0.1. *A Language and Environment for Statistical Computing*; R Foundation for Statistical Computing: Vienna, Austria, 2013; Volume 201, pp. 1–16.